Hindawi
Wireless Communications and Mobile Computing
Volume 2023, Article ID 6513526, 18 pages
https://doi.org/10.1155/2023/6513526

Research Article

Dual-Band Self-Complementary 5G Antenna for Wireless Body Area Network

H. M. Arifur Rahman,[1] **Md. Nakib Alam Shovon**,[1] **Mohammad Monirujjaman Khan**,[1] **and Turki M. Alanazi**[2]

[1]*Department of Electrical and Computer Engineering, North South University, Bashundhara, Dhaka-1229, Bangladesh*
[2]*Department of Electrical Engineering, College of Engineering, Jouf University, Sakaka, Saudi Arabia*

Correspondence should be addressed to Mohammad Monirujjaman Khan; monirujjamankhan1979bd@gmail.com

Received 10 July 2022; Revised 27 August 2022; Accepted 2 February 2023; Published 27 April 2023

Academic Editor: Kalidoss Rajakani

A design of a self-complementary dual-band fifth-generation (5G) antenna for a wireless body area network (WBAN) has been presented in this paper. Like many other advantages, dual-band antennas have the benefit of being able to establish a reliable wireless connection in places that are frequently out of reach. The antenna operates at two popular 5G NR, FR-2 frequency bands: n257, or 28 GHz, and n260, or 39 GHz. FR-2 bands are prominent for high-speed data transactions within a limited range, which is perfect for WBAN applications. The proposed self-complementary single element design has a physical size of 6 mm × 8 mm × 1.59 mm and is designed with a Rogers RT6002 substrate with a dielectric constant of 2.94. In free space simulations, the antenna performed satisfactorily, achieving around 90% efficiency and having return losses of 16.32 dB and 20.47 dB at the lower and upper frequency bands sequentially. The antenna generated almost omnidirectional patterns at both frequencies with a peak gain of 4.74 dB. By placing the antenna next to a 3D human torso phantom that had been digitally created with accurate human body features, the design's onbody performance was assessed. Onbody simulations produced favorable performance with a small dispersion from their peak values in some parameters, i.e., efficiency and reflection coefficients but produced more gains: 4.34 dBi at 28 GHz and 6.19 dBi at 39 GHz. For further distance-based investigation, the antenna was placed in five different positions relative to the torso. The test yields 67% efficiency with the minimum gap and 71% at the highest distance from the human body for the lowest band. Though the lower-frequency band produces better results with more gaps, the higher-frequency band performs consistently better in even the closest placement to the human body model by reaching more than 6 dB of gain with above 81% efficiency and wider than 10 GHz of bandwidth. The overall performance indicates this design can be a good solution to complex WBAN scenarios.

1. Introduction

The exponential growth of wireless communication as well as technological advancement is reflected by the extraordinary success of wireless mobile communications in recent years [1, 2]. The first generation's analog wireless communication supported only voice calls, which was introduced in the 1980s and evolved to the second generation's digitalized code-division multiple access (CDMA) and global system for mobile communication (GSM) telecommunication in 1991. In addition to voice calls, 2G offered short text messages and wireless internet access, limited to the 5 Kbps data transfer speed of general packet radio services, or GPRS, which had developed to a maximum of 48 kbps by enhanced data rates for GSM evolution, or in short, EDGE services [3]. The third generation of wireless communication, known as UMTS, which enabled higher data exchange rates through high-speed downlink packet access (HSDPA) and high-speed uplink packet access (HSUPA) and featured video chatting, did not arrive for ten more years. The commercial deployment of the fourth generation, referred to as long-term evolution (LTE) with Internet Protocol, or IP calling and worldwide interoperability for microwave access (WiMAX) [4], initially came in Oslo and Stockholm [5],

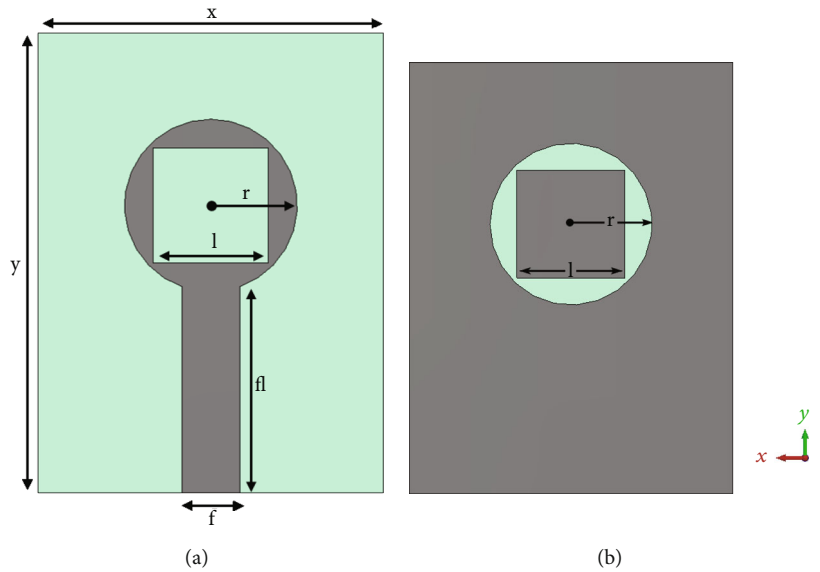

Figure 1: Antenna geometry: (a) top view and (b) bottom view.

but the stronger upgrade, LTE advanced (LTE-A), came in February 2011 with advanced multimedia featuring wireless broadband with a data rate up to 1 Gbps [6], which is ten times faster than regular LTE [7]. However, the fifth generation took only eight years to be introduced, as Chicago and Minneapolis were the first to experience 5G connectivity in April 2019 [8].

It is needless to say, antennas play a key element in wireless communication, and for the development of communication technology, antennas need to be more advanced and capable of performing the latest generation objectives. Given the importance of antenna systems for wireless technology and the accelerated growth of fifth-generation (5G) systems, it is essential for researchers to study and analyze them with great endeavor [9]. The radio access technology or air interface of the fifth-generation telecommunications network is referred to as 5G New Radio or more commonly 5G NR, which is separated into two sets of frequency bands. The first one is known as frequency range 1, or FR1, which covers from 600 MHz to 6 GHz, also known as SUB-6. The other one is FR-2, which is also known as the mmWave (millimeter wave) region of 5G bands. Both of these ranges include multiple frequency bands. The considerably weaker Ku or K-under Band, which experiences substantial atmospheric attenuation mostly because of water vapors, splits these two frequency sets [10]. The FR-2 range consists of six different frequency bands, ranging from 24.25 GHz to 48.20 GHz, named n257 to n262 [11]. Higher-frequency spectrum bands are more widely used and readily accessible for several purposes because many of them do not now have licenses. Six time division duplexing (TDD) bands with the letters n257 to n262 make up the FR2 spectrum. The two well-known bands among them are n257 and n260.

Many 4G LTE bands coexist with 5G channels inside the SUB6 frequency area. 5G bands, on the other hand, have an "n" prefix before their names, which makes them distinctive. For example, the n257 and n260 frequency bands are two

Table 1: Antenna dimension values.

Serial number	Parameter	Value (mm)
1	x	6
2	y	8
3	l	2.00
4	f	0.80
5	r	1.50
6	fl	3.55

Table 2: Antenna materials.

Parameter	Thickness (mm)	Material	Epsilon
Ground	0.035	PEC	—
Substrate	1.52	Rogers RT6002 (loss free)	2.94
Patch radiator	0.035	PEC	—

such 5G NR frequency bands that operate at 28 GHz and 39 GHz. These 5G FR2 bands fall under the microwave's Ka band and are very popular for their short-ranged, fast-paced data transmission, which is the primary specification for body-centric communication, or BCC. Body-centric networks (BCN), also known BAN, are a section of wireless communication with a lot of application potential. WBAN systems are gaining popularity in a number of fields, including biomedicine, the military, and business services [12–14]. In WBAN, wireless nodes are placed throughout the body and remain in communication with one another and a master node to exchange biological measurements that are then shared with an external database station or kept in the cloud [15, 16]. However, these BCN applications are very sensitive and require low-latency, fast-paced data connections for real-time monitoring. Meanwhile, to keep up with other

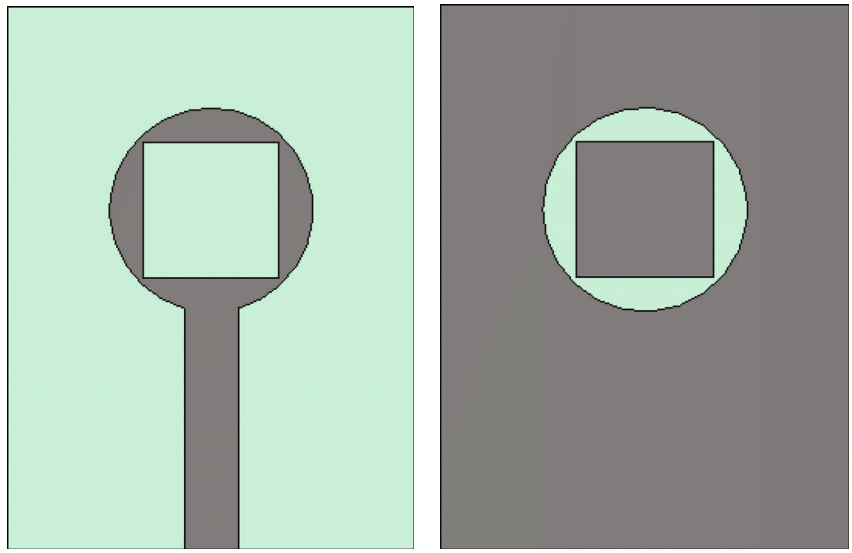

(a) (b)

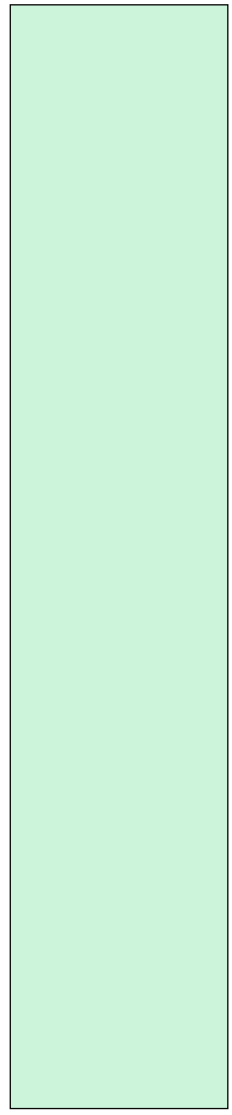

(c)

Figure 2: Continued.

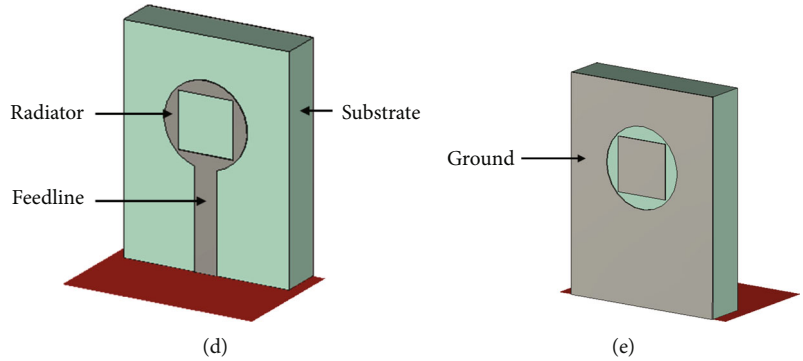

Figure 2: (a) Front view, (b) back view, (c) side view, (d) perspective front view, and (e) perspective back view.

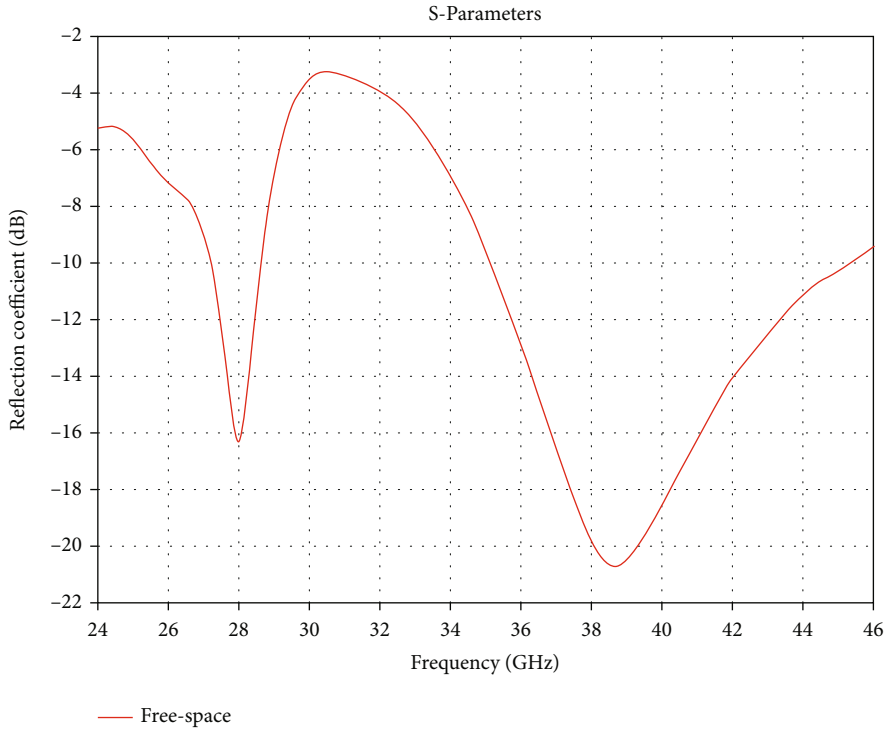

Figure 3: S-parameters for free-space.

forms of technological development, WBAN apparatus will need to be capable of exchanging large amounts of data in short periods of time.

A few recent studies in this similar field are promising. For instance, a dual-polarized, dual-band, stacked patch antenna was proposed by He et al. [17]. The antenna operates in the 5G bands of 28 GHz and 39 GHz, where the authors used capacitive coupled techniques to feed the antenna. The design recorded a simulated bandwidth of 3.4 GHz and 5.9 GHz on the lower and the higher band, respectively. Another dual-band microstrip patch antenna was presented by Sabek et al., operating at 28 GHz and 38 GHz [9]. The design contains stub-resonators to obtain resonant points. The authors claimed more than 94% of radiation efficiency was achieved by the antenna at both frequencies. Stanley et al. presented another dual-band, dual-polarized antenna [18], which is also a stacked patch millimeter wave antenna, similar to the [17]. This particular design has peak gains of 7.14 dBi and 6.44 dBi at 28 GHz and 39 GHz, respectively. Another dual-band antenna by Lai et al. operates at 28 GHz and 38 GHz and was made with the substrate integrated waveguide technique [19]. This slotted patch antenna element was also used to create an array to enhance performance. A dual-band antenna proposed for 5G applications by Ashraf et al. operates at the same frequency [20]. The printed slot antenna was designed with a band rejection element to obtain a notch at 33 GHz. Nhlengethwa and Kumar have proposed two multiband fractal microstrip patch antennas that operate at 2.4, 5.3, and 5.9 GHz [21].

In order to integrate wireless body area applications with traditional fifth-generation communications, a dual-band antenna for WBAN running at 5G mmWave frequencies might be extremely helpful. Dual-band antennas are

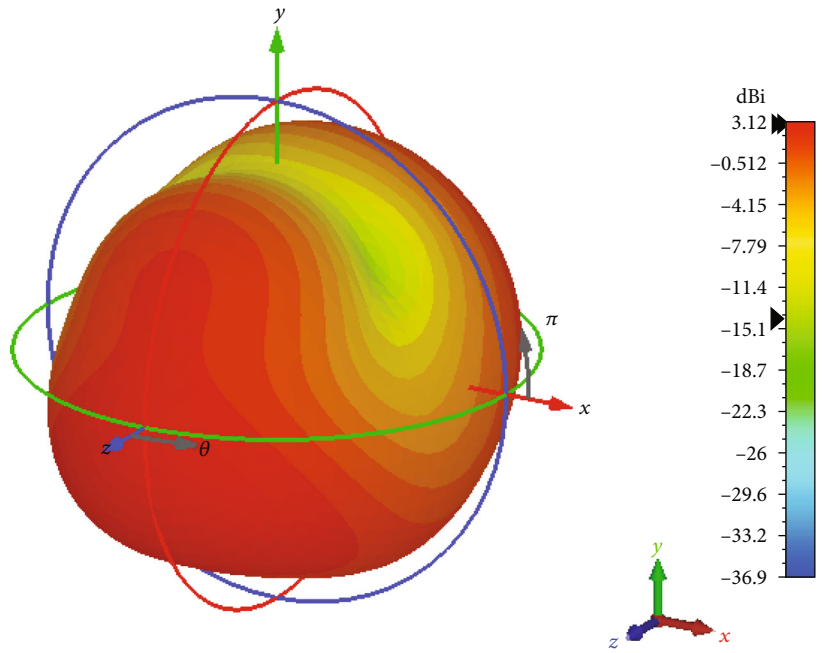

(a) 28 GHz

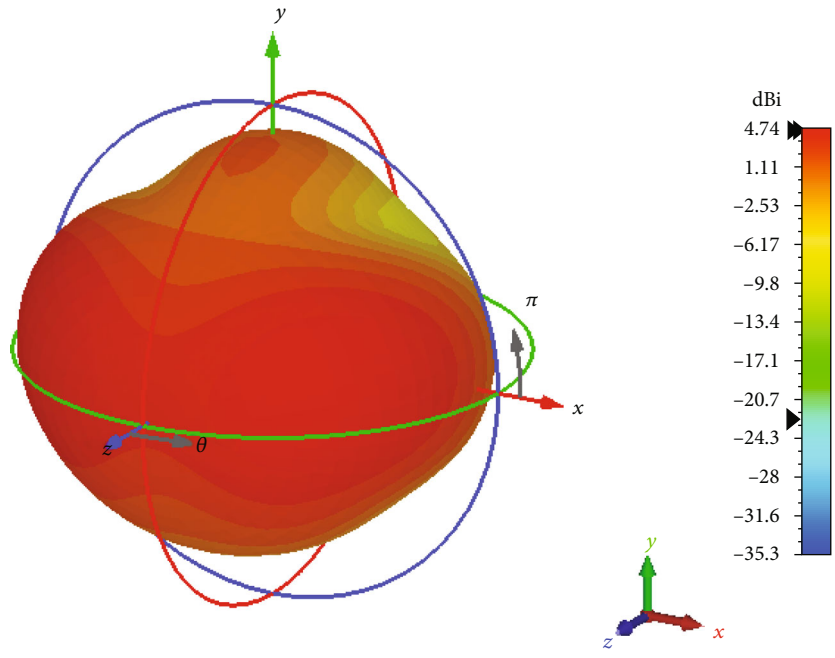

(b) 39 GHz

Figure 4: 3D radiation patterns in free space for 28 GHz and 39 GHz.

cost-efficient and work on multiple frequencies to keep a connection stronger [22], which can also save space and complexity by replacing two antennas operating at distinct frequencies. Motivated by these factors, a WBAN antenna operating at two separate 5G bands has been designed and its performance has been evaluated in the following sections of this paper. However, its novelty includes its multiple band operability, integration of 5G networks, and WBAN altogether. Additionally, this antenna is a very compact one with a wider bandwidth and sufficient gain with good efficiency in both onbody and offbody conditions. The first section introduces the generations of telecommunication with their histories, specifications, frequency bands of 5G, and prospective utilization of BCN with the existing latest generation of telecom networks. The second chapter shows the design technique of the antenna. The third and fourth sections present the free space results of the design and parametric studies, respectively. The fifth and sixth sections discuss the human onbody performance of the antenna distance-based analysis. The seventh section makes

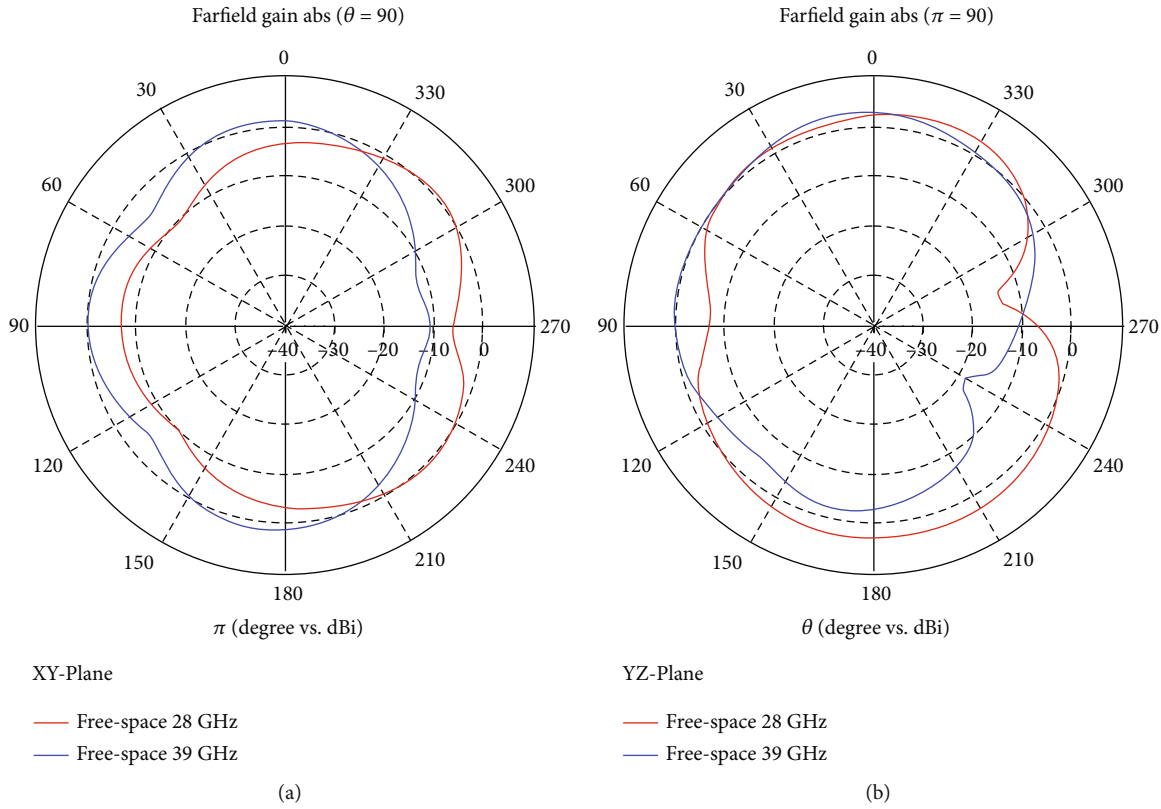

Figure 5: Free space 2D radiation pattern at 28 GHz and 39 GHz on the (a) XY plane and (b) YZ plane.

comparisons between the antenna parameters and current state-of-the-art designs, and the last portion draws conclusions.

2. Antenna Design

The proposed antenna was designed and simulated using the CST Microwave Studio Suite, a well-known electromagnetic element design and simulation application for Microsoft Windows. The antenna is built in a way that complements itself. The radiator patch of the antenna consists of a square slot enclosed by a circle. A circular patch helped to find the resonant point near the desired frequency, while a rectangular slot generated a notch in between two operating frequency bands. The antenna is 8 mm long and 6 mm wide with the substrate. The radius of the radiator's circular patch is 1.5 mm. The square hole has 2 mm long sides on each side. A feed line connects the primary circular shape to the waveguide port. The feed line is 3.55 mm long and has a width of $f = 0.8$ mm, which is symbolized by "fl" in Figure 1(a). The self-complementary design in the antenna's rear is depicted in Figure 1(b). On the backside of the antenna, there is a circular slot which is due to the self-complementary purpose. This circular slot at the backside of the antenna also contributes to the impedance matching of the antenna.

In Table 1, where "x" and "y" stand for the antenna's length and width, respectively, are the measurements of the various antenna parts. The values for the other parameters in Figure 1 are likewise included in the table (a).

Table 2 displays the materials, permittivity, and thickness of the various antenna layers. The patch radiator and the ground were both made of PEC (perfect electric conductor). Each layer is 0.035 millimeters thick. The Rogers RT6002 with a dielectric constant of 2.94 is used as the substrate for the antenna because of its exceptional dimensional stability and minimal loss at higher frequencies. Considering the higher resonant frequency, the electrical size of the antenna can be derived as $0.78\lambda \times 1.04\lambda \times 0.207\lambda$.The thickness of the substrate layer is 1.52 mm. The relative permittivity of the ground and radiator patches could not be measured because they are made of perfect electric conductors.

In Figure 2, the antenna is shown from a number of perspectives. Figure 2(a) and 2(b) show the antenna from the front and back, respectively. Figure 2(c) displays a side view of the antenna. Figure 2(d) and 2(e) represent the antenna front and back from a three-dimensional perspective view, with the various layers labeled.

3. Results of Free Space Simulations

3.1. Return Loss. In the 24 GHz to 46 GHz frequency band, the antenna was modeled in empty space. In the figure below, the frequency response is shown.

Figure 3 depicts the antenna's return loss response for the simulated frequency range. The resonance frequencies are 28 GHz and 39 GHz, respectively. From 27.21 GHz to 28.66 GHz and from 35.15 GHz to 45.34 GHz, the antenna becomes active with less than -10 dB reflection coefficient.

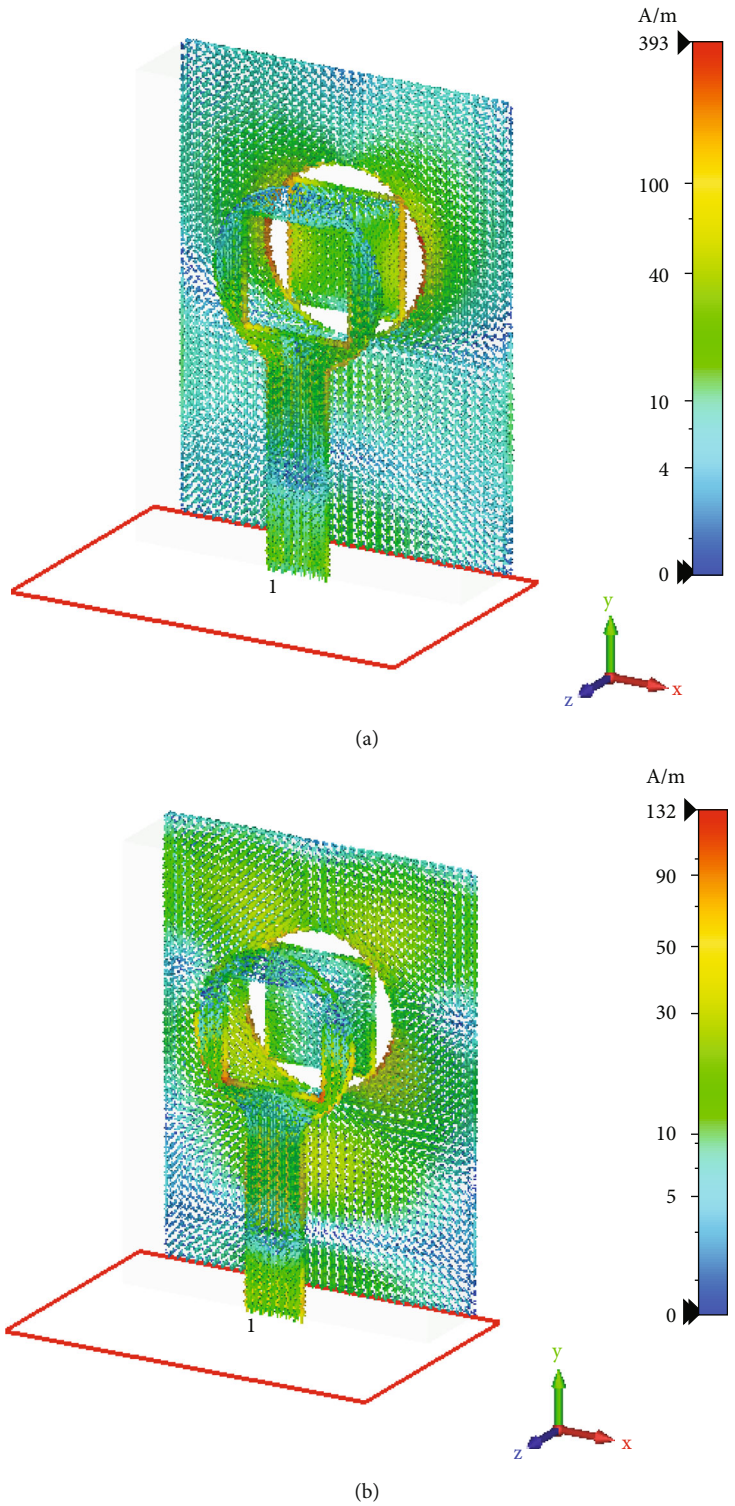

Figure 6: Surface current at (a) 28 GHz and (b) 39 GHz in empty space.

At 28 GHz, the value was -16.32 dB, while at 39 GHz, it was -20.47 dB. This antenna has good impedance matching at both operating frequencies.

3.2. 3D Radiation Patterns. The antenna's 3D radiation pattern at 28 GHz and 39 GHz are depicted in Figures 4(a) and 4(b), respectively. The antenna's maximum gains at 28 and 39 GHz are 3.124 dB and 4.743 dB, respectively. From Figures 4(a) and 4(b), it is noted that the 3D radiation patterns of this antenna at both operating frequency bands are nearly directive radiation to the Y direction. The radiation pattern of 39 GHz is more directive compared to that of 28 GHz, which results in more gain for the 39 GHz.

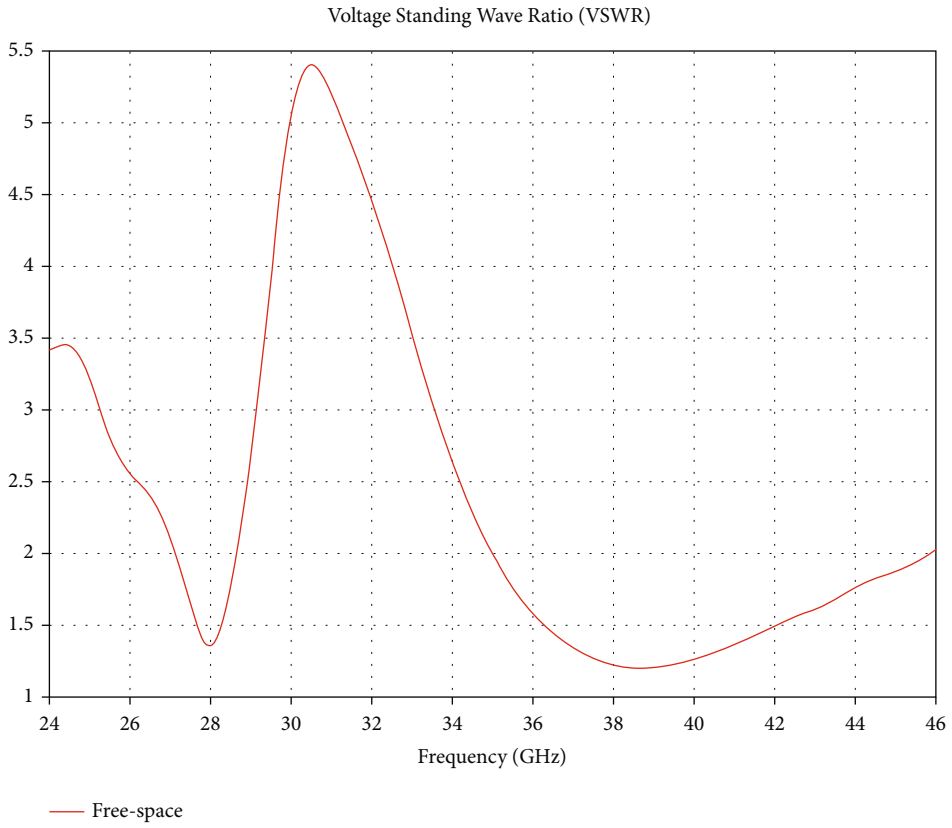

Figure 7: VSWR of the antenna in free space.

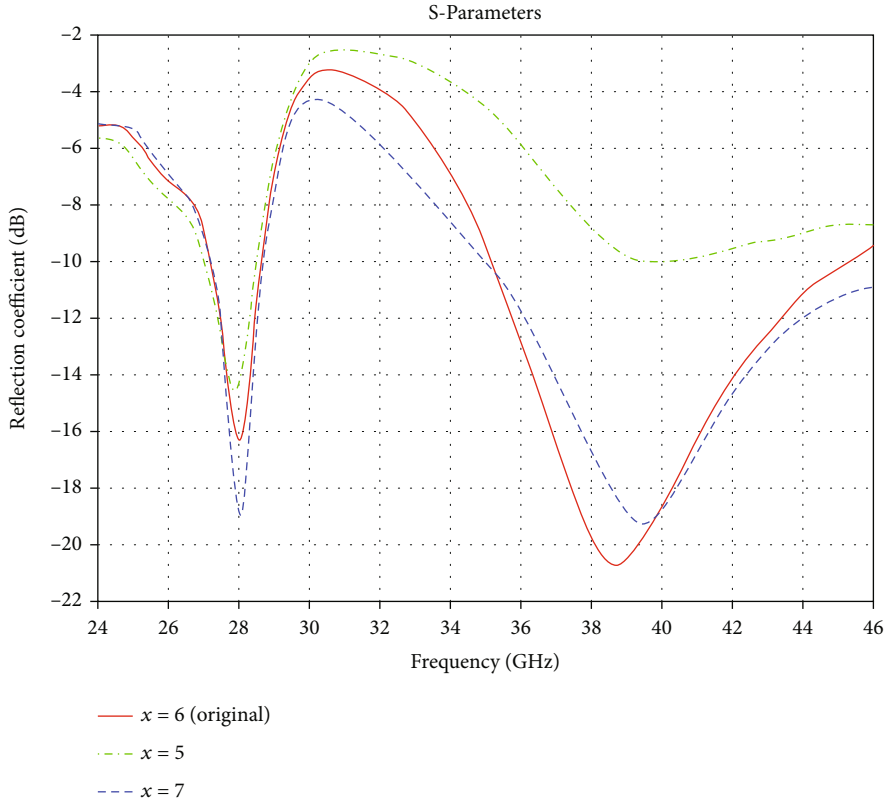

Figure 8: Reflection coefficient comparison with different "x" values.

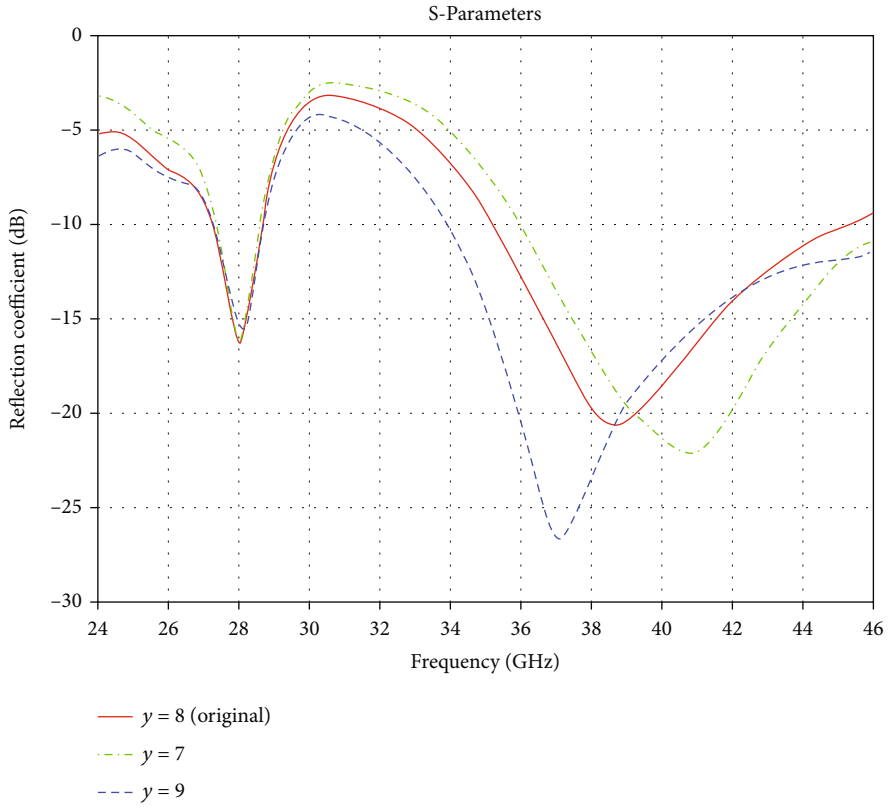

Figure 9: Reflection coefficients comparison with different "y" values.

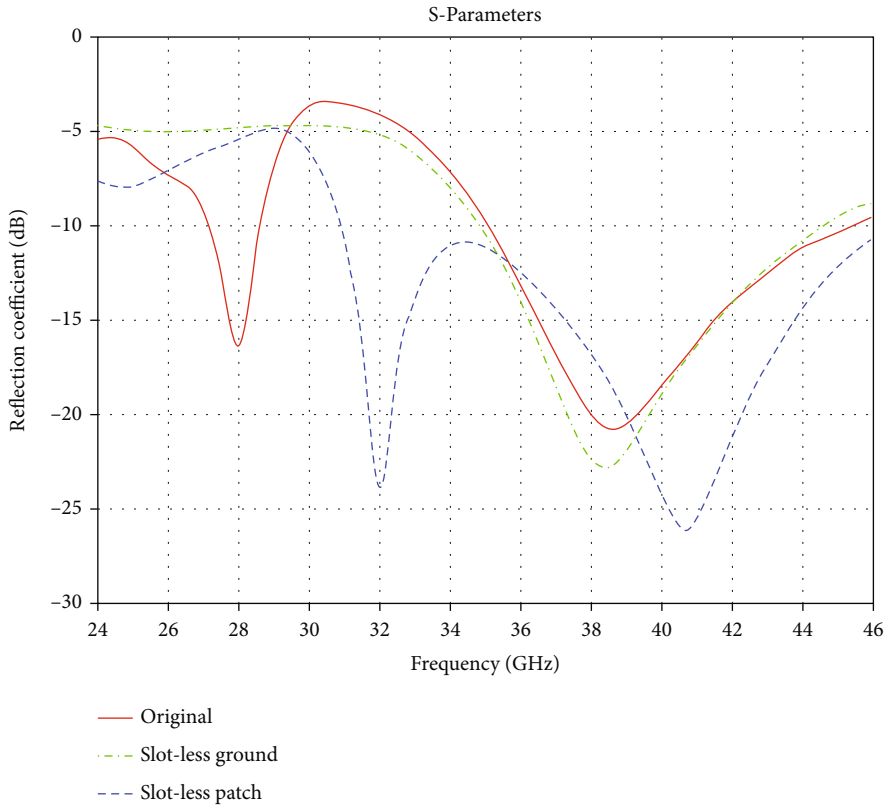

Figure 10: S-parameter comparison for designs with and without the slot.

Table 3: Parametric study.

Parameters		Reflection coefficient (dB)	Gain (dBi)	Radiation efficiency (%)	Impedance bandwidth (GHz)
Distance	Frequency				
Free space	28 GHz	-16.32	3.124	89.25	1.41
	39 GHz	-20.47	4.743	88.13	10.19
$x = 5$	28 GHz	-14.31	2.571	87.68	1.44
	39 GHz	-9.83	4.994	88.50	Null
$x = 7$	28 GHz	-18.94	3.332	91.50	1.47
	39 GHz	-18.98	4.103	83.87	—
$y = 7$	28 GHz	-16.30	2.894	86.39	1.25
	39 GHz	-19.76	5.119	90.80	—
$y = 9$	28 GHz	-15.48	3.226	91.72	1.41
	39 GHz	-19.40	5.641	85.88	—
Slot-less ground	28 GHz	-4.66	5.277	86.43	Null
	39 GHz	-22.01	4.922	87.17	9.53
Slot-less patch	28 GHz	-5.27	3.254	89.89	Null
	39 GHz	-19.73	4.550	88.38	—

3.3. 2D Radiation Patterns. Two-dimensional radiation patterns at 28 GHz and 39 GHz are shown in Figures 5(a) and 5(b), respectively, as the XY plane and the YZ plane. In the XY plane, the primary lobe of the antenna's radiation pattern is angled at a 90-degree angle. The major lobe orientation is roughly 180 degrees in the YZ plane pattern. In the YZ plane for both frequency bands in the back lobes, there is a null in the angles of 210 to 300 degrees. Figures 6(a) and 6(b) show the current distribution of the antenna.

3.4. Surface Current. When the antenna is powered by "port 1" at the 28 GHz and 39 GHz frequencies, Figure 7 depicts the distribution of surface current at those frequencies. At the radiator patch and the ground plane, the peak density reached 393 ampere/meter at 28 GHz and 132 ampere/meter at 39 GHz.

3.5. VSWR. The antenna's voltage standing wave ratio (VSWR) is shown in Figure 7. The VSWR number should continue to range between 1 and 2, with 1 being the ideal value and 2 being only slightly acceptable. At the resonant frequencies, the VSWR values are 1.36 and 1.209, respectively, which are close enough to the optimum value.

4. Parametric Study

After doing free space simulations using the aforementioned dimensions, parametric analysis was carried out to learn more about the nature of the design and how it affects the output results. This was done by altering the measurements, running new simulations, and comparing the results to the base results. Based on variations in the pertinent reflection coefficient or s11 curve, the parametric analysis was conducted.

To accomplish this, the antenna dimension was altered by altering the antenna's total size by altering the antenna substrate's width.

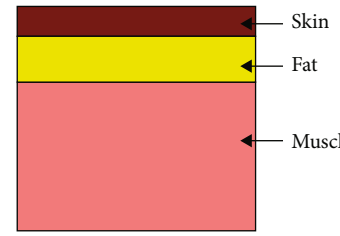

Figure 11: Torso phantom.

Figure 8 shows the calculated reflection coefficients for substrate width variations of 1 mm, first decreasing and then increasing. The green curve of the antenna indicates that when the substrate length is reduced to 5 mm, the resonance frequency at 28 GHz is somewhat pushed upward but does not work at 39 GHz. Increasing it to 7 mm (blue curve) results in a downward tilt at 28 GHz and an upward shift at 39 GHz. In the first instance, the curve found initially for the original design had higher return loss values at 28 GHz and 39 GHz. In the second scenario, return loss values decreased at 28 GHz but increased at 39 GHz in the second.

The substrate's length has now been modified in a manner similar to the original design. The substrate's length is initially cut down to 7 millimeters before being increased to 9 millimeters.

The return loss responses are shown in Figure 9 when the antenna substrate length is altered as previously mentioned. The green curve depicts the return loss with a 1 mm reduction in length. With the resonant point in this case at 39 GHz, the s11 curve is slightly right-shifted, but it is nearly unchanged at 28 GHz. The RL value, though slightly higher than the original design's value, is almost identical to the plot of the original design at 28 GHz. The resonant point shifts slightly to the left (blue curve) when the length is extended by 1 mm at 39 GHz, but virtually stays

Table 4: Torso phantom dimension values.

Parameter	Length (mm)	Width (mm)	Thickness (mm)	ε_r	Conductivity (S/m)
Skin	20	16	2	16.552	25.824
Fat	20	16	3	3.6985	1.6979
Muscle	20	16	10	24.44	33.609

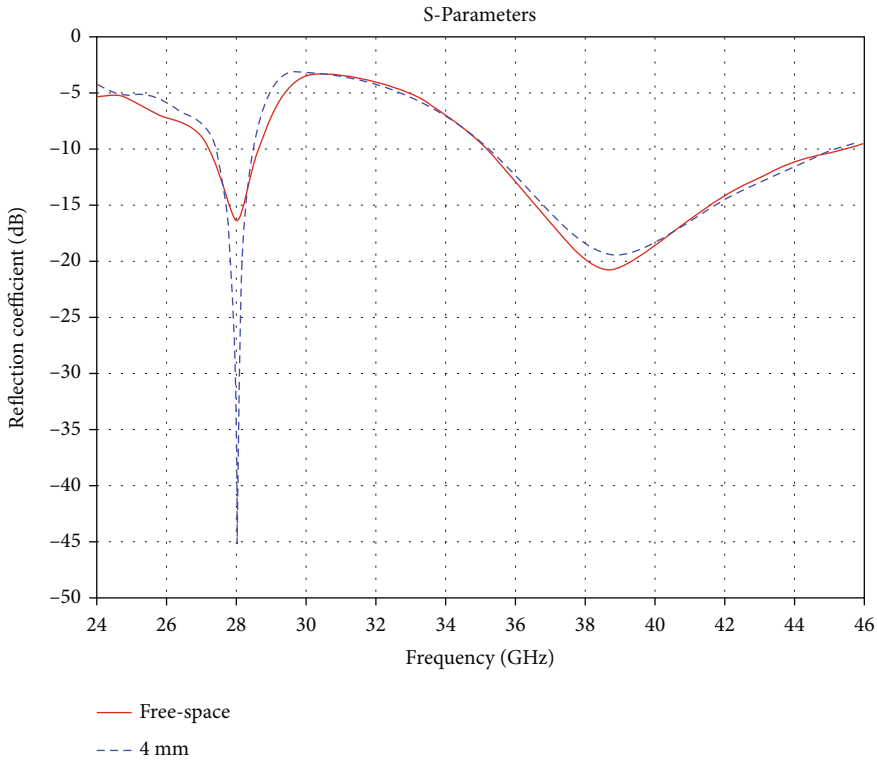

Figure 12: Comparison of the *S*-parameters in free space and on the body.

put at 28 GHz. For this scenario, the reflection coefficient is also increased at 39 GHz.

The antenna's slots are altered after the prior adjustments to determine how they impact the return loss curve. Both the radiator and the grounds have slots in the original. The simulation result was plotted after removing the slot from the ground. The return loss curve for the slot-less ground design is shown in Figure 10 by the green line. This curve shifts the curve upward to the inactive zone at 28 GHz and reduces the RL value, but it yields a better RL value at 39 GHz. After that, the radiator slot is removed. When the resonant point is pushed to the right for both frequencies in this scenario, the return loss is shown as a blue curve in the picture. At 28 GHz, the RL value is increased to the inactive zone, and at 39 GHz, it is also moderately increased.

4.1. Comparison. The table below provides a summary of the results of all the parametric investigations that were conducted previously. The results were contrasted with respect to gains, effectiveness, bandwidths, and return losses.

The results of the parametric study provided in Table 3 are the result of the aforementioned parametric investigation. The outcomes are contrasted with those from the free space simulation. When modifying the substrate's dimensions, it could not provide outcomes that were superior to the original plan. One instance involved a slot adjustment that decreased the return loss while moving the resonance frequency out of the desired range. As a result, for the frequencies of 28 GHz and 39 GHz, the original design produces more suitable and agreeable outcomes.

5. Onbody Performance Test

Because the antenna was designed for a WBAN application, it was tested on a computer-generated, three-dimensional model of a human torso. Muscle, fat, and skin were the three outermost components of the phantom. Figure 11 shows the three layers torso phantom. The muscle layer, which is deposited on top of the other two layers, is the layer with the greatest thickness, coming in at 10 millimeters. The fat layer is then placed between the muscle and the skin, with a thickness of 3 millimeters. Above the fat is the skin, which is the top

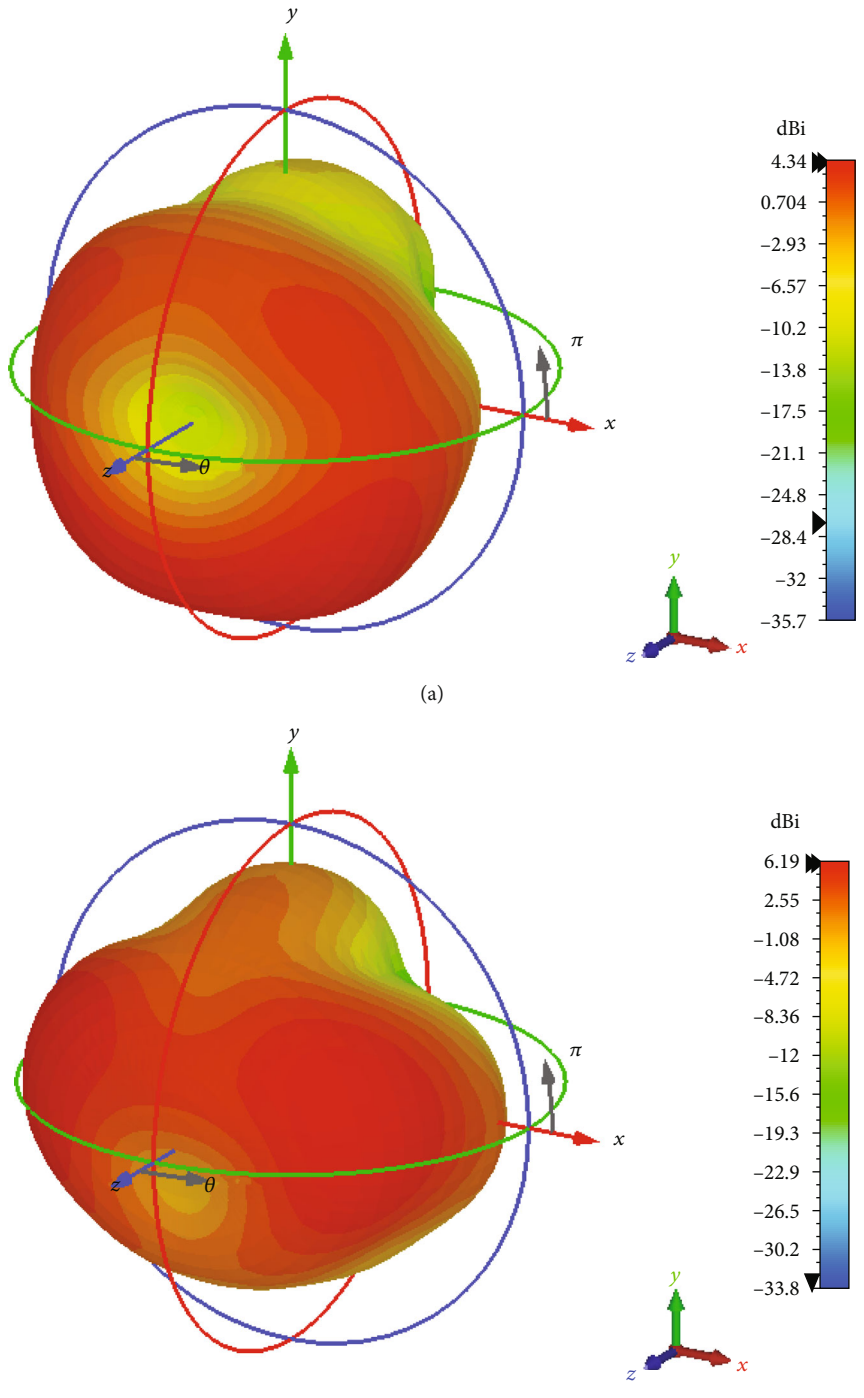

Figure 13: 3D radiation patterns for onbody with 4 mm gap at (a) 28GHz and (b) 39 GHz.

layer. Compared to the others, this layer is the thinnest. The thicknesses were chosen based on the average layer thicknesses in the human body. The electromagnetic properties of the layers are used to create them. The torso phantom, which is made up of these three layers, measures 20 mm in length and 16 mm in width. In Figure 10, the torso is depicted graphically. The results were then duplicated to make sure the slotted patch antenna was functioning properly before being put above the torso phantom. The results were then compared to a simulation conducted in free space. The table below shows the three layers of the torso phantom's dimensions and electromagnetic properties.

Table 4 gives a list of each layer's measurements individually. Materials used for the skin, fat, and muscle layers have corresponding relative permittivity values of 16.552, 3.6985, and 24.44. Siemens per meter is another unit used to express the material's conductivity.

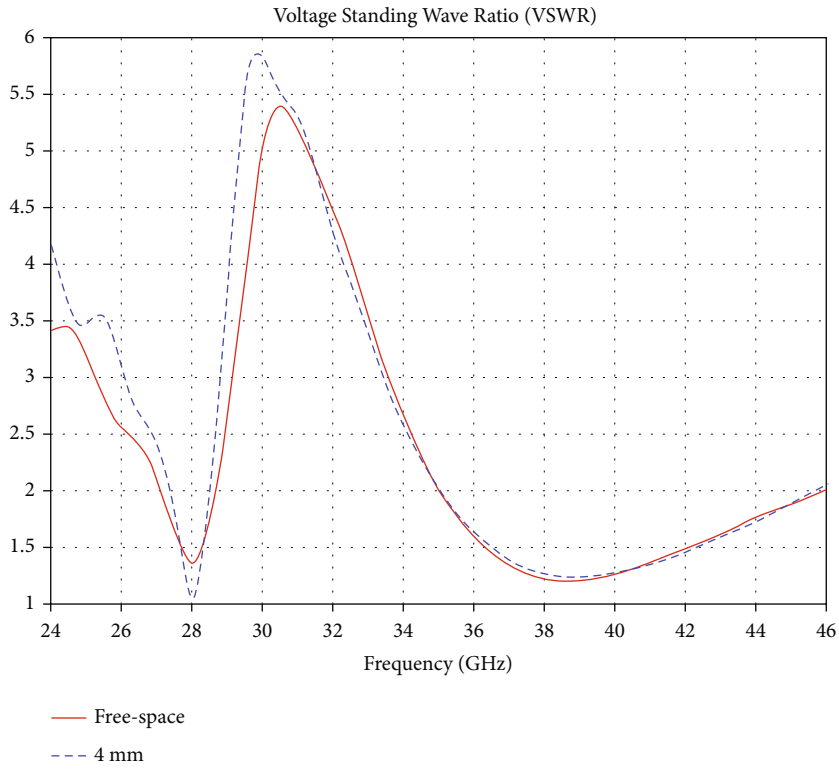

Figure 14: Free space and onbody VSWRs are compared.

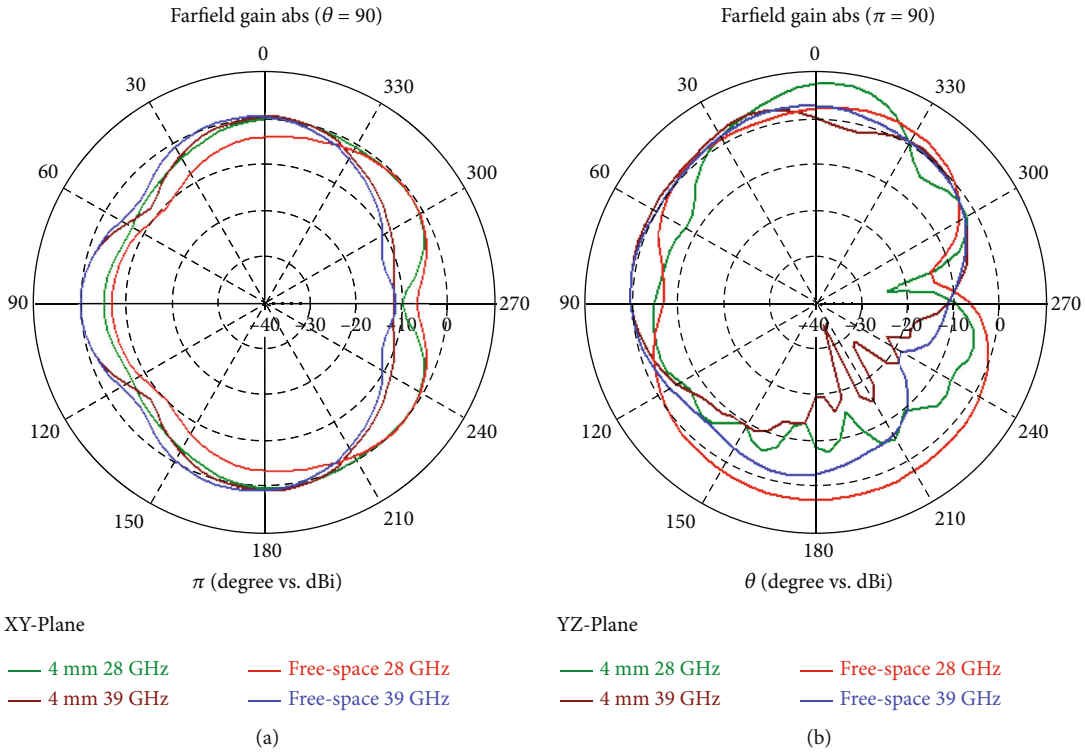

Figure 15: Comparison of the 2D radiation patterns at 4 mm in free space and on a body (a) on the XY plane and (b) on the YZ plane.

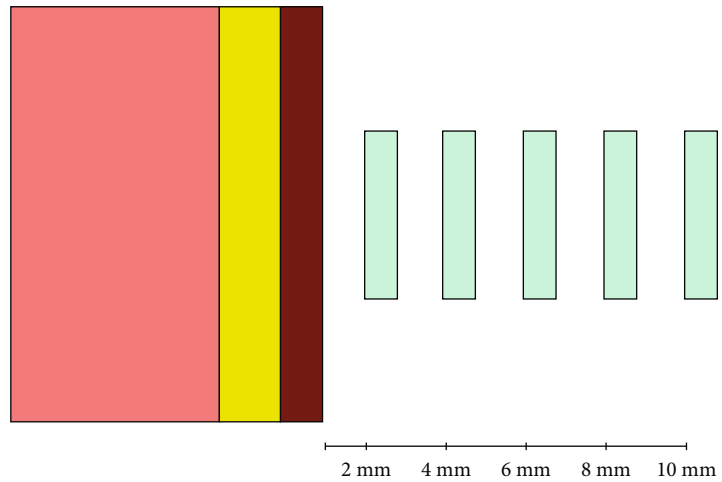

Figure 16: Right-side perspectives showing various onbody antenna positions.

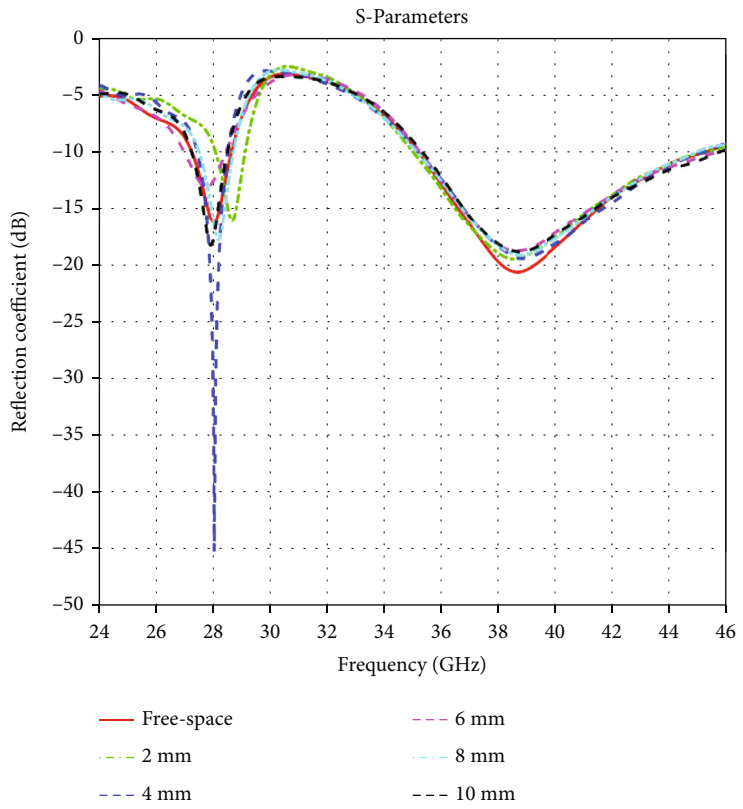

Figure 17: *S*-parameters comparison for various onbody distance.

5.1. Onbody Return Loss. Figure 12 shows the antenna's free space and onbody reflection coefficient. The onbody simulations were conducted at a common distance of 4 millimeters. The human body effect has significantly decreased the return loss value at 28 GHz while somewhat increasing it at 39 GHz. At a distance of 4 mm, it was found that the onbody bandwidth and the free space bandwidth are practically identical.

5.2. Onbody Radiation Pattern. A typical distance of 4 mm from the human torso was employed in the initial calculations for the antenna's onbody performance. A computed 3D far-field radiation pattern at 28 GHz and 39 GHz is displayed in Figure 13 when the suggested antenna is placed 4 mm from the torso phantom. The maximum gain was obtained along the z-axis at 4.34 dBi at 28 GHz and 6.19 dBi at 39 GHz. Compared to the free space 3D radiation patterns at both frequency bands of this antenna, the onbody radiation is more directive, which provides higher gains for the onbody case.

5.3. Onbody VSWR. Figure 14 depicts the antenna's onbody voltage standing wave ratio at a distance of 4 mm from the torso. The desired 28 GHz frequency for the onbody

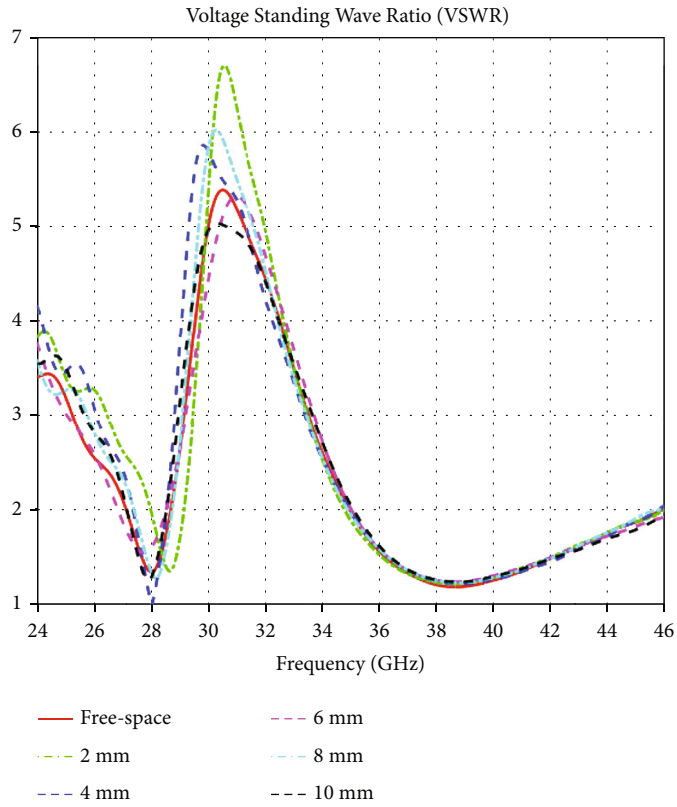

Figure 18: Comparison of the VSWR for various onbody distances.

simulation's VSWR value was found to be almost 1, which is the best outcome. The VSWR value at 39 GHz was found to be less than 1.4, which is acceptable as long as it is less than 2.

5.4. Onbody 2D Radiation Patterns. Figure 15 shows the antenna's 2D radiation patterns when it is 4 mm from a phantom of a human torso. The pattern in the XY plane is shown in Figure 15(a), and it shows how similar the onbody radiation pattern is to the pattern in free space. Very little distinguishes the lobes' gains and orientations. Figure 15 (onbody)'s pattern barely deviates from the expected free space result.

6. Distance-Based Study

The antenna was simulated over the torso at five various distances in order to better understand how it behaved on the human body. The torso phantom is isolated by 2 mm, 4 mm, 6 mm, 8 mm, and 10 mm [23].

As seen in Figure 16, the antenna was positioned at various heights above the body midsection. Several simulations were used for each distance to examine the antenna parameters, which were then compared with one another and the outcomes of the free space simulations.

Various distance based return loss curves have been plotted in Figure 17. The lowest return loss, which is just under -43 dB at 28 GHz, is achieved with an antenna positioned 4 mm from a person's torso. The comparison graph of the reflection coefficient shows that the return loss value varies between -9 dB and -18 dB at 28 GHz and between -18 dB and -20 dB at 39 GHz in all other cases. The bandwidths for all of the distinct onbody simulation situations are nearly identical, varying by roughly 1 GHz for both the 28 GHz and 39 GHz frequencies. Antenna parameters can still be used in a body-centric network despite the performance gaps between the open space S11 plot and the onbody return loss curves.

For onbody antenna installations at various ranges, Figure 18 examines the voltage standing wave ratios. As compared to free space data at 39 GHz, onbody VSWR curves for different distances display very similar results with only a few slight variations. The best VSWR at 28 GHz is practically 1 at a distance of 4 mm. However, in all instances, the VSWR was less than 1.5.

The radiation patterns are shown in Figure 19 to show how they change as the antenna is moved away from the body. The radiation patterns exhibit striking similarities with regard to primary lobes, maximum gains, and lobe orientations. Figures 19(a) and 19(b) depict the 2D radiation patterns of the antenna on XY planes at 28 GHz and 39 GHz, respectively, by adjusting the distance between the antenna and the human torso phantom. Even when the onbody distances are changed, the patterns remain remarkably stable. The lobe directions remained nearly unchanged, although the maximum gain values were slightly altered. Figures 19(c) and 19(d) show the patterns for YZ planes, which deviate from free space in some specific orientations.

Table 5 contrasts simulations conducted onbody and in free space. Several onbody simulations place the antenna at

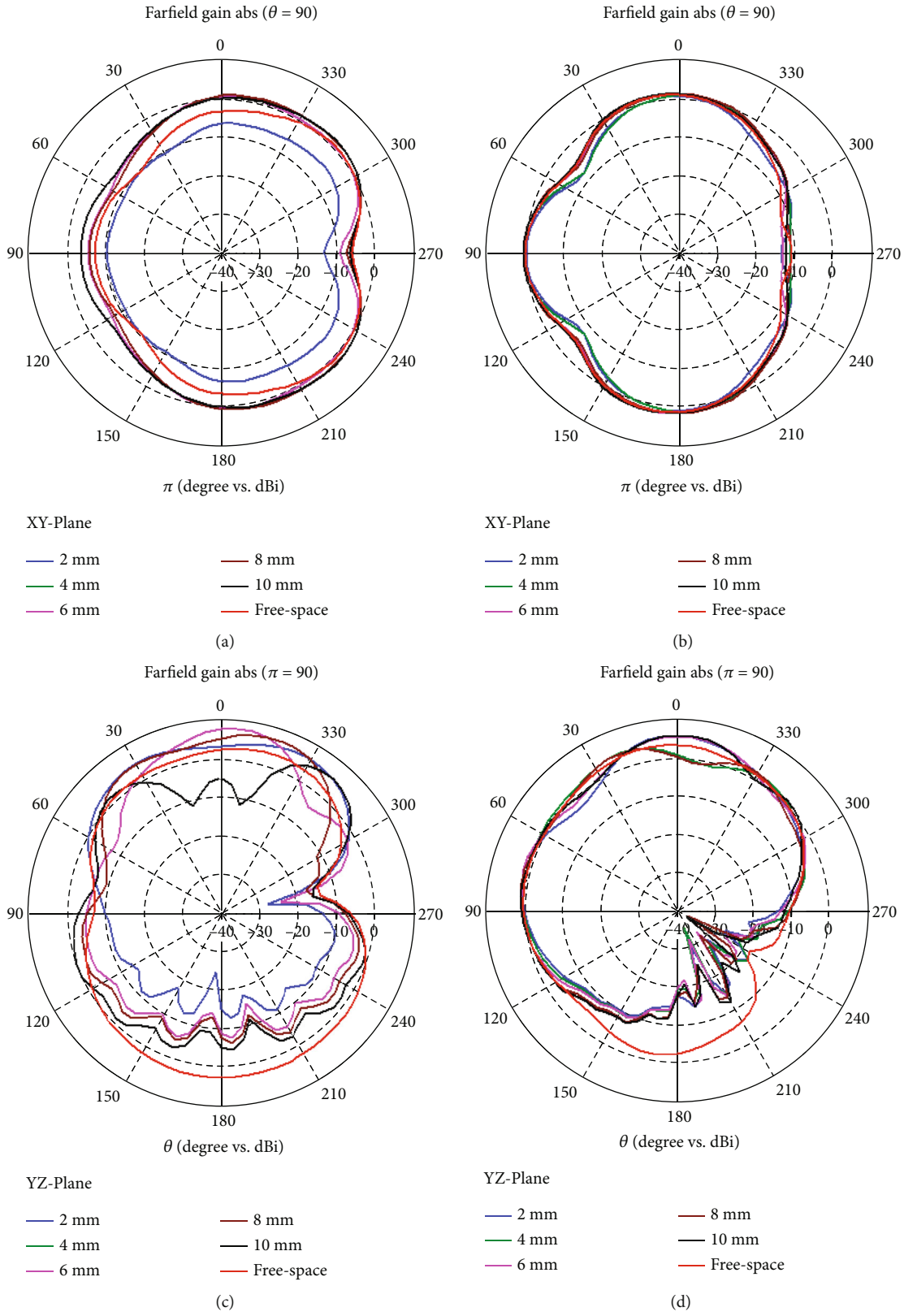

Figure 19: Comparison of 2D radiation patterns on the (a, b) XY and (c, d) YZ planes at 28 GHz and 39 GHz, for different onbody distances.

Table 5: Comparison parameters and results.

Parameters		Reflection coefficient (dB)	Gain (dBi)	Radiation efficiency (%)	Impedance bandwidth (GHz)
Distance	Frequency				
Free space	28 GHz	-16.32	3.124	89.25	1.41
	39 GHz	-20.47	4.743	88.13	10.19
2 mm	28 GHz	-9.67	5.925	67.08	Null
	39 GHz	-19.20	6.034	81.64	—
4 mm	28 GHz	-43.46	4.340	57.63	1.08
	39 GHz	-19.45	6.189	83.27	10.14
6 mm	28 GHz	-12.53	7.742	66.42	1.48
	39 GHz	-18.66	5.544	85.52	10.65
8 mm	28 GHz	-16.47	6.975	77.68	1.21
	39 GHz	-19.11	6.151	86.52	9.90
10 mm	28 GHz	-17.47	5.262	71.23	1.26
	39 GHz	-18.80	5.332	87.34	10.54

Table 6: Comparative analysis of various designs.

	Physical dimension (mm^2)	Reflection coefficient (dB)		Gain (dB)		Efficiency (%)		Bandwidth (GHz)	
		28 GHz	39 GHz	28 GHz	39 GHz	28 GHz	39 GHz	28 GHz	39 GHz
Design 1 [20]*	20 × 5.5	<-25	<-15	5.2	5.9	U/I	U/I	0.45	2.2
Design 2 [9]*	12 × 12	-28.1	-43.1	4.5	4.2	94	96.6	4.5	3.8
Design 3 [24]*	13 × 11.25	-23.6	-27.1	5.41	4.89	90.3	84.3	1.49	1.01
Design 4 [19]**	15.3 × 20.45	<-5	<-12.5	7.8	6.5	50	47	U/I	1.5
Design 5 (proposed)	6 × 8	-16.32	-20.47	3.124	4.743	89.25	88.13	1.41	10.19

*Data of higher frequency band at 38 GHz. **Approximate measured values.

intervals of 2 mm, 4 mm, 6 mm, 8 mm, and 10 mm from the torso phantom. The comparison takes bandwidth, radiation effectiveness, return loss, and gain into account. The return loss comparison shows that the lowest reflection coefficient, with values of -43.46 dB at 28 GHz and -19.45 dB at 39 GHz, is found at a distance of 4 mm from the torso phantom. The antenna was placed 6 mm from the body model to obtain the highest gain at 28 GHz and 8 mm from the body model to achieve the highest gain at 39 GHz.

At 28 GHz, the radiation efficiencies are saturated at various distances. Radiation efficiencies, on the other hand, gradually improve as the antenna is moved away from the human body at 39 GHz. For 6 mm distances, the widest bandwidth was discovered at 28 GHz, and for 4 mm distances, the widest bandwidth was found at 39 GHz. The lossy human body tissues are to blame for the discrepancies in the free space and onbody results in this investigation. Human body tissues are dispersive over the frequency, so different variations of antenna performance are noticed in both bands.

7. Comparison with Other Designs

A comparison table of the onbody performance of the proposed antenna and a few additional antennas designed for BAN/BCN systems operating at 28 GHz and 39 GHz can be found below. For comparison's sake, a standard 4 mm distance was measured from the torso phantom of a human body.

In the abovementioned Table 6, various current, recent dual-band 5G antennas' parameters were contrasted with those of the suggested antenna for onbody testing. For Designs 1, 2, and 3, data of the higher-frequency band was given for their corresponding resonant frequency (38 GHz) instead of 39 GHz. The data for Design 4 has been taken for the single element. However, multiple element arrays of the design showed excellent results in their experiments. The proposed design is physically more compact than the other concepts in Table 6. Though the design has slightly lower gains than others, it has almost 90 percent of efficiency in both frequency bands with wider bandwidths.

8. Conclusion

Dual-band antennas are beneficial and provide many more advantages than single-band antennas. Dual-band antennas have the benefit of being able to establish a reliable wireless connection in places that are frequently out of reach. It also provides a cost-effective solution by using a single-element antenna for multiple frequency bands instead of using multiple single element designs for multiple bands. Similarly, wireless equipment may face several acute conditions when it is supposed to be used very close to the human body. The dielectric properties of human body materials differ from those of free space, causing wireless signals to degrade. For this reason, a dual-band antenna enables multipurpose

solutions in critical scenarios, making them more popular among wireless device manufacturers.

The presented antenna design exhibited respectable onbody performance and was impressive in free space simulations. The antenna demonstrated a peak gain of 6.189 dB with more than 83 percent efficiency in its higher band with an average gap of 4 mm from the body. The bandwidth was also greater than 10 GHz for both onbody and offbody cases. Even for the closest simulated distance, it achieved more than 6 dBi of gain with around 82% efficiency. The antenna can also be used where a band rejection notch is required between 29 GHz and 32 GHz. For many similar reasons, this antenna can be a suitable candidate for WBAN applications.

Data Availability

The data used to support the findings of this study are freely available at http://niremf.ifac.cnr.it/tissprop/.

Conflicts of Interest

The authors declare that they have no conflicts of interest to report regarding the present study.

Acknowledgments

The authors are thankful for the support from the North South University CTRG Research Grant (CTRG-21-SEPS/24), North South University, Bashundhara, Dhaka-Bangladesh.

References

[1] D. Mikulić, E. Šopp, D. Bonefačić, and Z. Šipuš, "Textile slotted waveguide antennas for body-centric applications," *Sensors*, vol. 22, no. 3, p. 1046, 2022.

[2] P. Kumar, T. Ali, and A. Sharma, "Flexible substrate based printed wearable antennas for wireless body area networks medical applications (review)," *Radioelectronics and Communications Systems*, vol. 64, no. 7, pp. 337–350, 2021.

[3] 3GPP - A global Initiative, "The mobile broadband standard," Available at: "https://www.3gpp.org/technologies/keywords-acronyms/102-gprs-edge".

[4] A. Hashimoto, H. Yorshino, and H. Atarashi, "Roadmap of IMT-advanced development," *IEEE Microwave Magazine*, vol. 9, no. 4, pp. 80–88, 2008.

[5] Telia Company, "First in the world with 4G," About the company / History; Available at: "https://www.teliacompany.com/en/about-the-company/history/first-in-the-world-with-4g/".

[6] I. Daudov, M. Sygotina, and V. Nadrshin, "Principles of the transition from 4G LTE to 5G," *Journal of Physics: Conference Series*, vol. 2032, no. 1, article 012006, 2021.

[7] 4G LTE Advanced, "Electronics notes," Available on https://www.electronics-notes.com/articles/connectivity/4g-lte-long-term-evolution/what-is-lte-advanced.php.

[8] News Center, *When was 5G introduced?*Verizon News Archives2019, Available online, https://www.verizon.com/about/our-company/5g/when-was-5g-introduced.

[9] A. Sabek, A. Ibrahim, and W. Ali, "Dual-band millimeter wave microstrip patch antenna with StubResonators for 28/38 GHz applications," *Journal of Physics: Conference Series*, vol. 2128, no. 1, article 012006, 2021.

[10] J. du Preez and S. Sinha, *Millimeter-Wave Antennas: Configurations and Applications*, Springer, 2016.

[11] Y. Lee, B. Kim, and H. Shin, "28-GHz CMOS direct-conversion RF transmitter with precise and wide-range mismatch calibration techniques," *Electronics*, vol. 11, no. 6, p. 840, 2022.

[12] A. Gupta, M. Tripathi, and A. Sharma, "A provably secure and efficient anonymous mutual authentication and key agreement protocol for wearable devices in WBAN," *Computer Communications*, vol. 160, pp. 311–325, 2020.

[13] M. Arefin, M. Ali, and A. Haque, "Wireless body area network: an overview and various applications," *Journal of Computer and Communications*, vol. 5, no. 7, pp. 53–64, 2017.

[14] K. Kwon, J. Ha, S. Lee, and J. Choi, "Design of a dual-band onbody antenna for a wireless body area network repeater system," *International Journal of Antennas and Propagation*, vol. 2012, Article ID 350797, 5 pages, 2012.

[15] S. Ahmad, A. Ghaffar, N. Hussain, and N. Kim, "Compact dual-band antenna with paired L-shape slots for on- and off-body wireless communication," *Sensors*, vol. 21, no. 23, p. 7953, 2021.

[16] H. A. Sabti and D. V. Thiel, "A study of wireless communication links on a body centric network during running," *Procedia Engineering*, vol. 72, pp. 3–8, 2014.

[17] Y. He, M. Rao, Y. Liu, G. Jing, M. Xi, and L. Zhao, "28/39-GHz dual-band dual-polarized millimeter wave stacked patch antenna array for 5G applications," in *2020 International Workshop on Antenna Technology (iWAT)*, pp. 1–4, Bucharest, Romania, 2020.

[18] M. Stanley, Y. Huang, H. Wang et al., "A dual-band dual-polarised stacked patch antenna for 28 GHz and 39 GHz 5G millimetre-wave communication," in *2019 13th European Conference on Antennas and Propagation (EuCAP)*, pp. 1–4, Krakow, Poland, 2019.

[19] F.-P. Lai, L.-W. Chang, and Y.-S. Chen, "Miniature dual-band substrate integrated waveguide slotted antenna array for millimeter-wave 5G applications," *International Journal of Antennas and Propagation*, vol. 2020, Article ID 6478272, 2020.

[20] N. Ashraf, O. Haraz, M. A. Ashraf, and S. Alshebeili, "28/38-GHz dual-band millimeter wave SIW array antenna with EBG structures for 5G applications," in *2015 International Conference on Information and Communication Technology Research (ICTRC)*, pp. 5–8, Abu Dhabi, United Arab Emirates, 2015.

[21] N. Nhlengethwa and P. Kumar, "Fractal microstrip patch antennas for dual-band and triple-band wireless applications," *International Journal on Smart Sensing and Intelligent Systems*, vol. 14, no. 1, pp. 1–9, 2021.

[22] S. Soundarya, S. Meghana, and P. Shanthi, "Design of dual band micro strip antenna for 2.4 GHz and 3.6 GHz," *International Journal of Recent Technology and Engineering (IJRTE)*, vol. 8, no. 1, 2019.

[23] M. M. Khan, H. M. Rahman, M. Shovon et al., "Design and analysis of a 5G wideband antenna for wireless body-centric network," *Wireless Communications and Mobile Computing*, vol. 2022, Article ID 1558791, 16 pages, 2022.

[24] A. Muhammad, I. K. Muhammad, M. O. Syed, A. K. Abbas, and S. Asif, "Design and analysis of millimeter wave dielectric resonator antenna for 5G wireless communication systems," *Progress in Electromagnetics Research C*, vol. 98, pp. 239–255, 2020.